analytical chemistry

pubs.acs.org/ac Article

# $Fe_3C$-Assisted Single Atomic Fe Sites for Sensitive Electrochemical Biosensing

Xiaoqian Wei,[‖] Shaojia Song,[‖] Weiyu Song, Weiqing Xu, Lei Jiao, Xin Luo, Nannan Wu, Hongye Yan, Xiaosi Wang, Wenling Gu, Lirong Zheng, and Chengzhou Zhu*

Cite This: *Anal. Chem.* 2021, 93, 5334−5342 Read Online

ACCESS | Metrics & More | Article Recommendations | Supporting Information

**ABSTRACT:** The rational construction of advanced sensing platforms to sensitively detect $H_2O_2$ produced by living cells is one of the challenges in both physiological and pathological fields. Owing to the extraordinary catalytic performances and similar metal coordination to natural metalloenzymes, single atomic site catalysts (SASCs) with intrinsic peroxidase (POD)-like activity have shown great promise for $H_2O_2$ detection. However, there still exists an obvious gap between them and natural enzymes because of the great challenge in rationally modulating the electronic and geometrical structures of central atoms. Note that the deliberate modulation of the metal−support interaction may give rise to the promising catalytic activity. In this work, an extremely sensitive electrochemical $H_2O_2$ biosensor based on single atomic Fe sites coupled with carbon-encapsulated $Fe_3C$ crystals ($Fe_3C$@C/Fe−N−C) is proposed. Compared with the conventional Fe SASCs (Fe−N−C), $Fe_3C$@C/Fe−N−C exhibits superior POD-like activity and electrochemical $H_2O_2$ sensing performance with a high sensitivity of 1225 $\mu A/mM \cdot cm^2$, fast response within 2 s, and a low detection limit of 0.26 $\mu M$. Significantly, sensitive monitoring of $H_2O_2$ released from living cells is also achieved. Moreover, the density functional theory calculations reveal that the incorporated $Fe_3C$ nanocrystals donate electrons to single atomic Fe sites, endowing them with improved activation ability of $H_2O_2$ and further enhancing the overall activity. This work provides a new design of synergistically enhanced single atomic sites for electrochemical sensing applications.

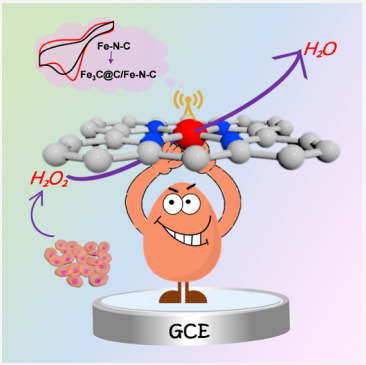




$H_2O_2$ has been increasingly considered as a significant mediator for physiology, aging cell activation, and disease in organisms. Therefore, the quantitative detection of $H_2O_2$ in biological conditions, especially intracellular is of great significance.[1,2] Especially, electrochemical biosensors based on a natural enzyme, horseradish peroxidase (HRP), perfectly combine the excellent activity of enzymes with the advantage of the electrochemical method, such as rapid response and good quantitative ability, providing an easy way to achieve signal amplification, and the sensitive and selective detection of $H_2O_2$.[3] Nevertheless, the high cost, environmental instability and the limited direct electron transfer between electrodes and the redox center due to the insulate protein shells of HRP immensely hinder its wider applications. Alternatively, nanomaterials with intrinsic peroxidase (POD)-like activity have been reported as alternatives of the natural enzyme for the reduction of $H_2O_2$,[4−7] while most of them usually exhibit limited sensitivity compared to natural enzymes, which cannot meet the requirement of practical applications.

Owing to the 100% atomic utilization efficiency and extraordinary catalytic performances, single atomic site catalysts (SASCs) have been illustrated to possess attractive catalytic performances in a variety of reactions.[8−13] Different from conventional nanoparticle catalysts, the metal−support interactions of SASCs are most prominent as the size of metal sites decreases to the atomic level.[14−18] Consequently, the modulation of the local coordination environment has potential to optimize the electronic and geometric structures of metal atoms. Especially, the introduction of some synergistic components is expected to improve the catalytic performance of SASCs. For example, local coordination atoms, heteroatoms, and other metal atoms have been proposed to modulate the local environment of single atomic sites.[19−21] Among them, single atomic sites coupling with metal nanoparticles/nanoclusters are considered to exhibit excellent catalytic activity than the corresponding SASCs.[22−25] For example, Fe−$Fe_3C$ nanoparticles were reported to improve the performance of single atomic Fe sites toward the oxygen reduction reaction through the modification of adsorption strength between the single atomic Fe site and the OH* intermediate.[23] Similar to oxygen reduction, the reduction of $H_2O_2$ also involves the adsorption/desorption process of oxygen-containing intermediates on active sites, whose strength determines their catalytic activity and the sensitivity of the electrochemical

**Received:** February 10, 2021
**Accepted:** March 9, 2021
**Published:** March 18, 2021

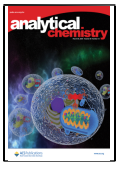




https://doi.org/10.1021/acs.analchem.1c00635
*Anal. Chem.* 2021, 93, 5334−5342

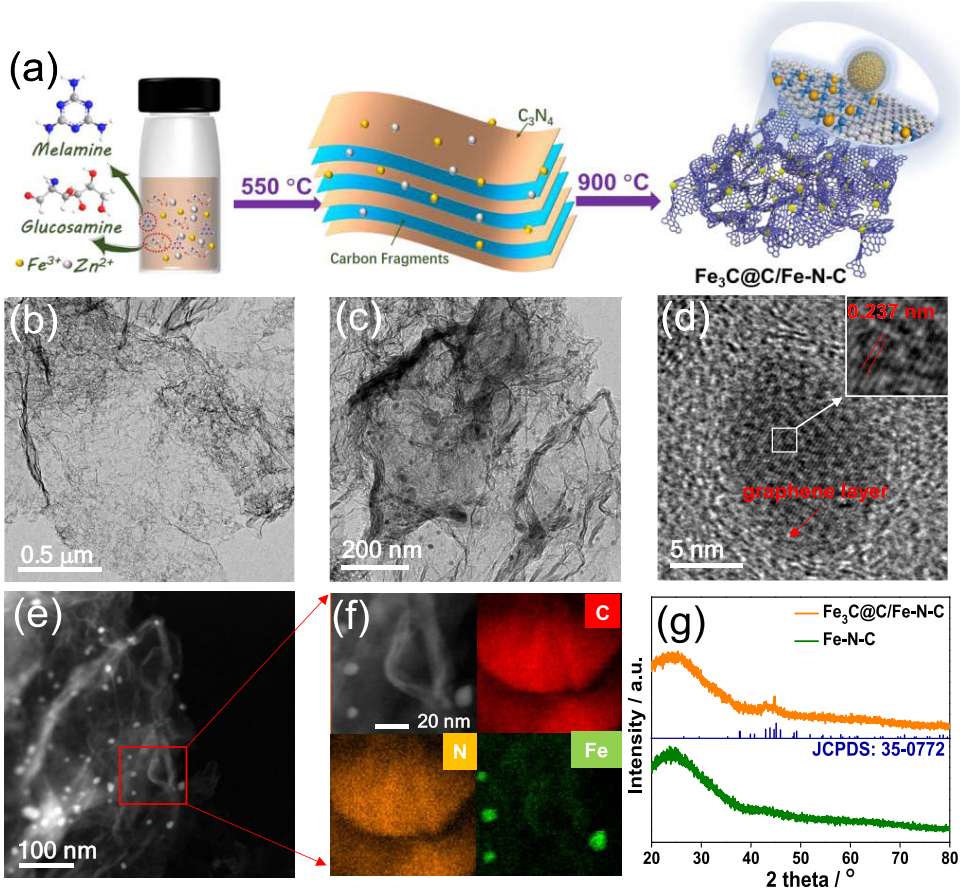


**Figure 1.** (a) Schematic illustration of the synthesis process of $Fe_3C$@C/Fe−N−C. TEM (b, c) and HRTEM images (d) of $Fe_3C$@C/Fe−N−C. HAADF-STEM images (e) and the corresponding EDS element mappings (f) of $Fe_3C$@C/Fe−N−C. (g) XRD patterns of $Fe_3C$@C/Fe−N−C and Fe−N−C.

sensors. Inspired by this, synergistically enhanced SASCs may hold great promise to serve as substitutes for natural enzymes to achieve higher sensitivity detection of cellular $H_2O_2$.

In this work, the catalyst of single atomic Fe sites coupled with carbon-encapsulated $Fe_3C$ crystals ($Fe_3C$@C/Fe−N−C) was synthesized through a one-step $C_3N_4$ spatial confinement strategy. As expected, $Fe_3C$@C/Fe−N−C showed excellent POD-like activity, exhibiting a much higher performance to detect $H_2O_2$ than Fe SASCs (Fe−N−C). The $Fe_3C$@C/Fe−N−C-based electrochemical sensor shows superior sensitivity and selectivity with a limit of detection (LOD) of 0.26 $\mu$M and a response time of 2 s. Furthermore, the density functional theory (DFT) calculations demonstrate that the superior activity of $Fe_3C$@C/Fe−N−C is ascribed to the relatively lower adsorption barriers of $H_2O_2$ molecules on single atomic Fe sites than that of Fe−N−C due to the assistance of $Fe_3C$ nanocrystals. As a concept application, the $Fe_3C$@C/Fe−N−C-based biosensor was established for sensitive electrochemical detection of intracellular $H_2O_2$, which holds great promise in biosensing applications.

## EXPERIMENTAL PROCEDURE

**Synthesis of $Fe_3C$@C/Fe−N−C.** In a typical procedure, 1.2 g of glucosamine and 6 g of melamine were dispersed in 25 mL of water and stirred vigorously for 10 min. Then, 5 mL of a solution containing 0.811 g of $FeCl_3{\cdot}6H_2O$ and 0.818 g of $ZnCl_2$ was injected into the above solution, followed by vigorous stirring for 2 h at room temperature. The as-obtained precipitates were freeze-dried and ground to a fine powder. Subsequent annealing was carried out under a $N_2$ flow with a ramp rate of 5 °C/min at 900 °C and maintaining for 2 h to obtain $Fe_3C$@C/Fe−N−C. Typically, $Fe_3C$@C/Fe−N−C was stirred in 2 M $H_2SO_4$ at 80 °C for 48 h. The obtained $Fe_3C$ nanocrystals were removed and were denoted as Fe−N−C. The synthesis process of $Fe_3C$@C is similar to that of $Fe_3C$@C/Fe−N−C and the carbon precursor is glucose, replacing melamine and glucosamine to avoid the introduction of the N source. C−N was also prepared similar to $Fe_3C$@C/Fe−N−C, except for the addition of the Fe precursor.

**Characterizations.** The morphology of various catalysts was evaluated by transmission electron microscopy (TEM, Titan G260-300). X-ray photoelectron spectroscopy (XPS) measurements were performed by a Thermo ESCALAB 250XI (Thermo Fisher), and all of the binding energy data were calibrated by C 1s (284.6 eV). A D8 ADVANCE (Bruker, Germany) was used to obtain X-ray diffraction (XRD) characterization. Raman spectra were obtained using a Renishaw 1000 microRaman system. Aberration-corrected high-angle annular dark-field scanning transmission electron microscopy (AC-HAADF-STEM) was performed by a Titan G2−600 (FEI). The pore parameters such as the Brunauer−Emmett−Teller (BET) specific surface area and the Barrett−Joyner−Halenda (BJH) pore-size distribution were measured using $N_2$ adsorption/desorption at 77 K on a MICROMERITICS ASAP 2460 (MICROMERITICS). Hydrophilicity was investigated by determining the contact angle using a


https://doi.org/10.1021/acs.analchem.1c00635
Anal. Chem. 2021, 93, 5334−5342

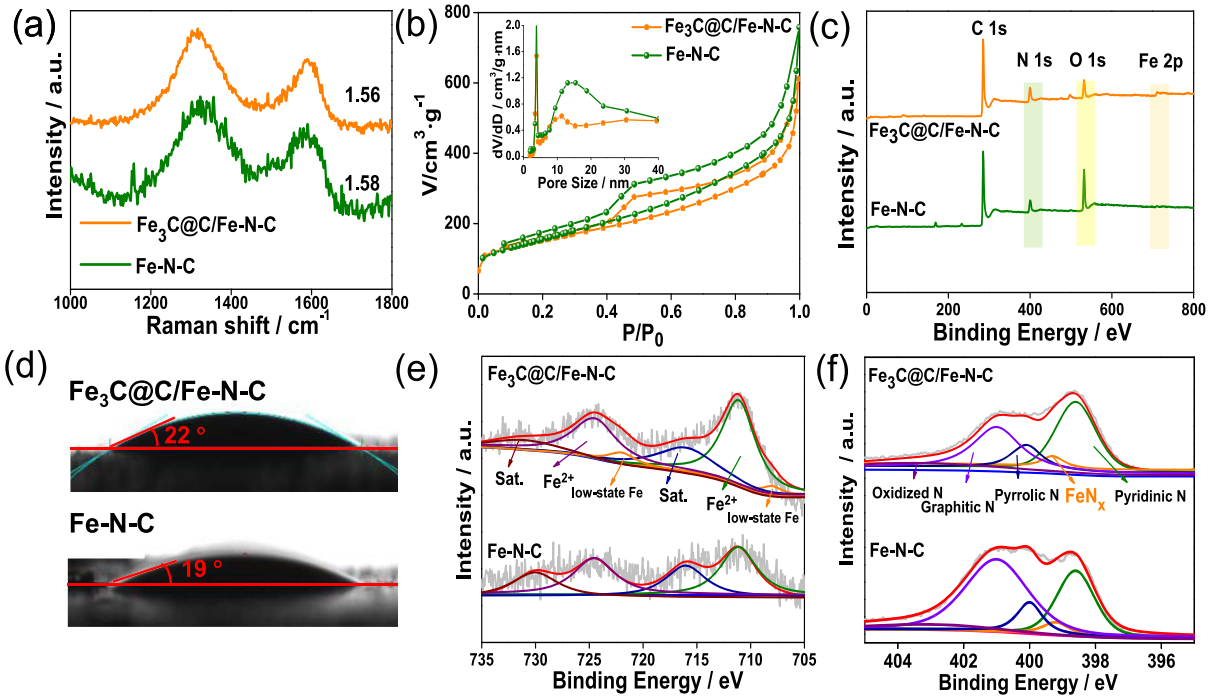


**Figure 2.** Raman spectra (a), $N_2$ adsorption/desorption isotherms (b), full XPS spectra (c), contact angle (d), and high-resolution XPS spectra of Fe 2p (e) and N 1s (f) of $Fe_3C$@C/Fe−N−C and Fe−N−C (the inset in (b) shows the corresponding pore-size distribution of the catalysts determined from the BJH method).

DSA30 (Krüss, German). The X-ray absorption fine structure spectra (Fe K-edge) were collected on a 1W1B station at Beijing Synchrotron Radiation Facility (BSRF).

**Fabrication of the $H_2O_2$ Sensor.** 4 mg of the catalyst was dispersed into 1 mL of a mixture of water, ethanol, and 5 wt % Nafion (the volume ratio is 49:50:1), followed by ultrasonic treatment for 30 min to prepare the catalyst ink. Before the modification, the glassy carbon electrode (GCE, 0.07 $cm^2$) was polished with 1.0, 0.3, and 0.05 mm alumina slurry to make its surface mirror like and then rinse thoroughly with deionized water. Then, 3 $\mu$L of the catalyst ink was dropped on the GCE and dried at 55 °C. For comparison, Fe−N−C, $Fe_3C$@C and C−N were fabricated using a similar procedure.

**Cell Culture.** The Dulbecco's modified Eagle's medium was used to culture the Hell cells under oxidative stress conditions supplemented with fetal bovine serum (10%) and then maintained in a humidified atmosphere of 5% $CO_2$ at 37 °C.

**Electrochemical Detection of $H_2O_2$ Released from Cells.** Hela cells were seeded and grown in a cell culture plate with a diameter of 35 mm ($1.0 \times 10^6$ cells). The cell number was estimated by a cell counter. The culture medium was removed and the cells were washed with the deoxygenated PBS buffer (0.01 M, pH 7.4) three times. Then, 3 mL of $N_2$-saturated PBS (0.1 M, pH 7.4) was added for electrochemical measurements. The GCE modified with $Fe_3C$@C/Fe−N−C was immersed in the cell solution and used for the amperometric detection of $H_2O_2$ in Hela cells. When phorbol-12-myristate-13-acetate (PMA) (20 $\mu$L, 2 $\mu$M) was injected into the solution, it can motivate the cells to release $H_2O_2$ into PBS. The proposed electrochemical biosensing platform can respond to $H_2O_2$ in real time.

**Computational Method.** The density functional theory (DFT) calculations were performed using Vienna ab initio Simulation Package (VASP). The Perdew−Burke−Enrzerhof (PBE) parametrization of the generalized gradient approximation (GGA) was used to describe the electronic exchange-correlation energies. In this study, the $H_2O_2$ reduction activity on the three models including $FeN_4$ and $FeN_4/Fe_3C$ was investigated. The criterion of total energy convergence in the optimization of the atomic structure is $10^{-5}$ eV, the convergence criterion of the atomic force is 0.05 eV/Å, and the cut off energy of plane wave expansion is 400 eV. Considering the Coulomb interactions in Fe d-states, a Hubbard correction was added ($U_{eff}$ = 3 eV for the d-states of Fe atoms). The Brillouin zone was sampled using the Monkhorst−Pack method with 2 × 2 × 1 $k$-point meshes. The surface models after geometry optimization are shown in Figure S17.

The adsorption energies of $H_2O_2$ were calculated according to $\Delta E_{H_2O_2} = \Delta E_{H_2O_2}{}^* - E_{surface} - \Delta E_{H_2O_2}$. Here, $\Delta E_{H_2O_2}$ is the surface with the adsorbed $H_2O_2$ molecules, while $E_{surface}$ and $\Delta E_{H_2O_2}$ represent the energies of the surface model and the $H_2O_2$ molecules, respectively.

## RESULTS AND DISCUSSION

To obtain $Fe_3C$@C/Fe−N−C, a facile $C_3N_4$ spatial confinement strategy was proposed, where melamine can be transformed to $C_3N_4$ at about 550 °C and served as a template (Figure 1a). On the one hand, $C_3N_4$ templates induce the carbon fragments derived from glucosamine to form thin carbon nanosheets, which can contribute to the exposure of the active centers and mass/electron transfer during the catalytic process (Figures 1b and S1).[26] On the other hand, the $C_3N_4$ template and $Zn^{2+}$ restrain the agglomeration of Fe species into large and irregular Fe nanoparticles, thus contributing to the production of well-defined $FeN_x$ and $Fe_3C$ species. It can be speculated that $Fe_3C$ may be derived from the reduction of $Fe^{3+}$ by C during the pyrolysis process and then embed into the graphene layer.[22] As illustrated in Figures 1c and S2, highly


https://doi.org/10.1021/acs.analchem.1c00635
Anal. Chem. 2021, 93, 5334−5342

uniform nanocrystals with an average size of 7.5 nm are observed. A high-resolution TEM (HRTEM) image identifies that the lattice spacing of these nanocrystals is around 0.237 nm, in accordance with the (211) facet of the $Fe_3C$ species (Figure 1d). Besides, there exist thin graphene layers encapsulating around $Fe_3C$ species, providing strong protection for them. The high-angle annular dark-field scanning transmission electron microscopy (HAADF-STEM) image and corresponding energy-dispersive spectroscopy (EDS) mappings of $Fe_3C$@C/Fe−N−C (Figure 1e, 1f) reveal the existence of $Fe_3C$@C nanocrystals. Besides, rich Fe and N species are also observed, which can be ascribed to the $FeN_x$ species. Typically, to verify the role of $Fe_3C$ species, a selective etching strategy is adopted to remove $Fe_3C$ species, leaving only single atomic Fe sites (named Fe−N−C).[27] The clear holes in TEM images of Fe−N−C shown in Figure S3 confirm the disappearance of $Fe_3C$ species. XRD patterns in Figure 1g show that $Fe_3C$@C/Fe−N−C exhibits clear characteristic peaks of $Fe_3C$ species, while all of these peaks disappear in Fe−N−C, indicating the successful removal of $Fe_3C$ species.

Figure 2a shows the Raman spectra of the as-prepared catalysts. At 1350 and 1580 $cm^{-1}$, there are two main peaks, representing the defects (D band) and planar motion of $sp^2$-carbon atoms (G band) in graphite carbon, respectively.[28] Both Fe−N−C and $Fe_3C$@C/Fe−N−C exhibit high $I_D/I_G$ ratios, demonstrating the rich defective structures. The $N_2$ adsorption−desorption isotherms and pore-size distributions determined from the BJH method are displayed in Figure 2b and Table S1. Due to the removal of $Fe_3C$ species, Fe−N−C exhibits a larger BET surface area (550.93 $m^2/g$) than $Fe_3C$@C/Fe−N−C (523.35 $m^2/g$). Typically, pore-rich structures and large surface areas play a critical role in the exposure of the active sites and high mass transfer efficiency.[29] Figure 2c shows the full XPS spectra of $Fe_3C$@C/Fe−N−C and Fe−N−C. After the removal of $Fe_3C$ species, the content of Fe in Fe−N−C is much lower than that of $Fe_3C$@C/Fe−N−C (Table S2). Notably, the rich O and N species of the catalysts are favorable to the access of dissolved $H_2O_2$ to the active sites by improving the hydrophilicity according to the contact angle measurement, enhancing the sensitivity detection (Figures 2d and S4).[30] From the deconvoluted Fe 2p spectra shown in Figure 2e, two peaks are identified to be located at 710.9 and 724.5 eV, assigned to Fe $2p_{3/2}$ and Fe $2p_{1/2}$, respectively. Especially, there exist extra peaks for $Fe_3C$@C/Fe−N−C compared to Fe−N−C at 708 eV and 722.5 eV, representing a low-valent state of Fe in $Fe_3C$ moieties.[23] The deconvoluted XPS N 1s spectra can be fitted into pyridinic-N (398.6 eV), $FeN_x$ (399.3 eV), pyrrolic-N (400.1 eV), graphitic-N (401.0 eV), and oxidized-N (403.3 eV), respectively, and both $Fe_3C$@C/Fe−N−C and Fe−N−C possess rich $FeN_x$ moieties (Figure 2f). In addition, high-resolution XPS spectra of C 1s were also recorded, where the $sp^3$-C percentages of Fe−N−C and $Fe_3C$@C/Fe−N−C are 25.5 and 22.69%, demonstrating the high defective level (Figure S5).[31]

The single atomic Fe atoms were further detected by the AC-HAADF-STEM measurement. Numerous light dots are observed for $Fe_3C$@C/Fe−N−C, which can be attributed to the Fe element (Figure 3a). Note that both ultrafine Fe clusters and single atomic Fe sites can be distinguished from Figure 3b (partially marked by yellow and red circles) and these Fe clusters can be vested to $Fe_3C$ species according to the HRTEM. Furthermore, X-ray absorption near edge structure (XANES) and Extended X-ray absorption fine

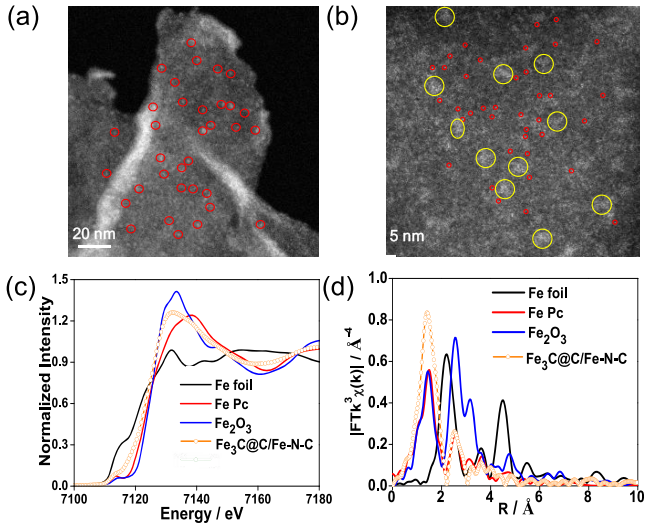


**Figure 3.** (a, b) AC-HAADF-STEM images of $Fe_3C$@C/Fe−N−C. XANES (c) and EXAFS (d) curves of $Fe_3C$@C/Fe−N−C and references at the Fe K-edge.

structure (EXAFS) measurements were performed to insightfully expound the characteristics of the local electronic and geometric structures of Fe atoms. As illustrated in Figure 3c, the position of the absorption of the Fe K-edge in $Fe_3C$@C/Fe−N−C is situated between that of the Fe foil and FePc, implying the positive charges between 0 and +2 of the Fe element.[32] Note that the signal from the Fe−N contribution (1.5 Å) is observed in the EXAFS spectrum of $Fe_3C$@C/Fe−N−C. Besides, there also exists a clear peak between 2 and 3, suggesting the presence of the Fe−Fe peak.[33] As shown in Figure S6, the Fe−Fe characteristic peak of Fe−N−C has disappeared, demonstrating the removal of $Fe_3C$ species. To confirm the coordination configuration of the single atomic Fe site, the EXAFS fitting was carried out on Fe−N−C. The experimental and fitting results are listed in Table S3 and the coordination number ($N$) of Fe is calculated to be about 5.9. Note that these Fe−O bonds may be derived from the O species in the measuring environment and easy to be removed during the catalytic process.[34,35]

To verify the POD-like property of $Fe_3C$@C/Fe−N−C and better understand the role of $Fe_3C$@C in the catalytic efficiency, a typical chromogenic reaction was conducted, where 3,3′,5,5′-tetramethylbenzidine (TMB) can be used as a substrate and oxidized to the oxidation state of TMB (oxTMB) with blue color in the presence of $H_2O_2$ (Figure 4a). As expected, the POD-like performance of $Fe_3C$@C/Fe−N−C is much higher than that of Fe−N−C, indicating that $Fe_3C$@C plays a critical role in the POD-like activity of $Fe_3C$@C/Fe−N−C (Figure 4b). As shown in Figure S7, the absorbance value at 652 nm increased with the reaction time. Figure 4c shows that the specific activity (SA) of $Fe_3C$@C/Fe−N−C is 2.27-fold higher than that of Fe−N−C.[36] To further probe the catalytic activity of $Fe_3C$@C/Fe−N−C, the Michaelis−Menten kinetics was measured toward $H_2O_2$ (Figure 4d). Especially, the Michaelis−Menten constant ($K_m$) value of $Fe_3C$@C/Fe−N−C ($8.58 \times 10^{-7}$ M/s) is lower than that of Fe−N−C ($9.68 \times 10^{-7}$ M/s), indicating that $Fe_3C$@C/Fe−N−C possesses a higher affinity toward $H_2O_2$. Moreover, the $V_{max}$ value of $Fe_3C$@C/Fe−N−C toward $H_2O_2$ (2.82 mM) is also higher than that of Fe−N−C (1.53 mM) (Table S4). Based on these results, the introduction of $Fe_3C$@C is


https://doi.org/10.1021/acs.analchem.1c00635
Anal. Chem. 2021, 93, 5334−5342

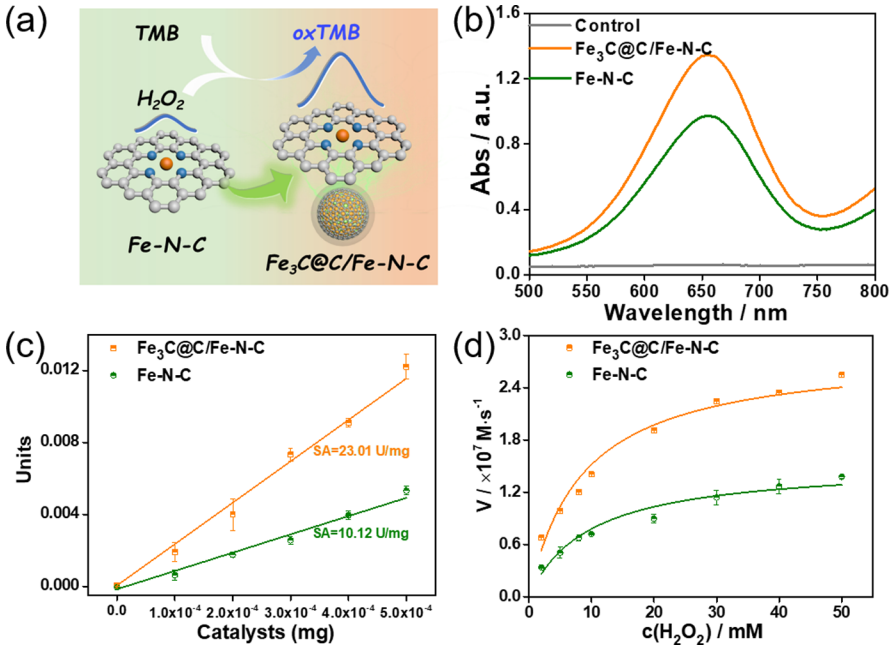


**Figure 4.** (a) Schematic diagram of $Fe_3C$@C/Fe−N−C and Fe−N−C to mimic catalytic activity of POD. (b) The absorbance spectra of the TMB chromogenic reaction catalyzed by $Fe_3C$@C/Fe−N−C and Fe−N−C. (c) Specific activities of $Fe_3C$@C/Fe−N−C and Fe−N−C. (d) Steady-state kinetics curves of $Fe_3C$@C/Fe−N−C and Fe−N−C toward $H_2O_2$.

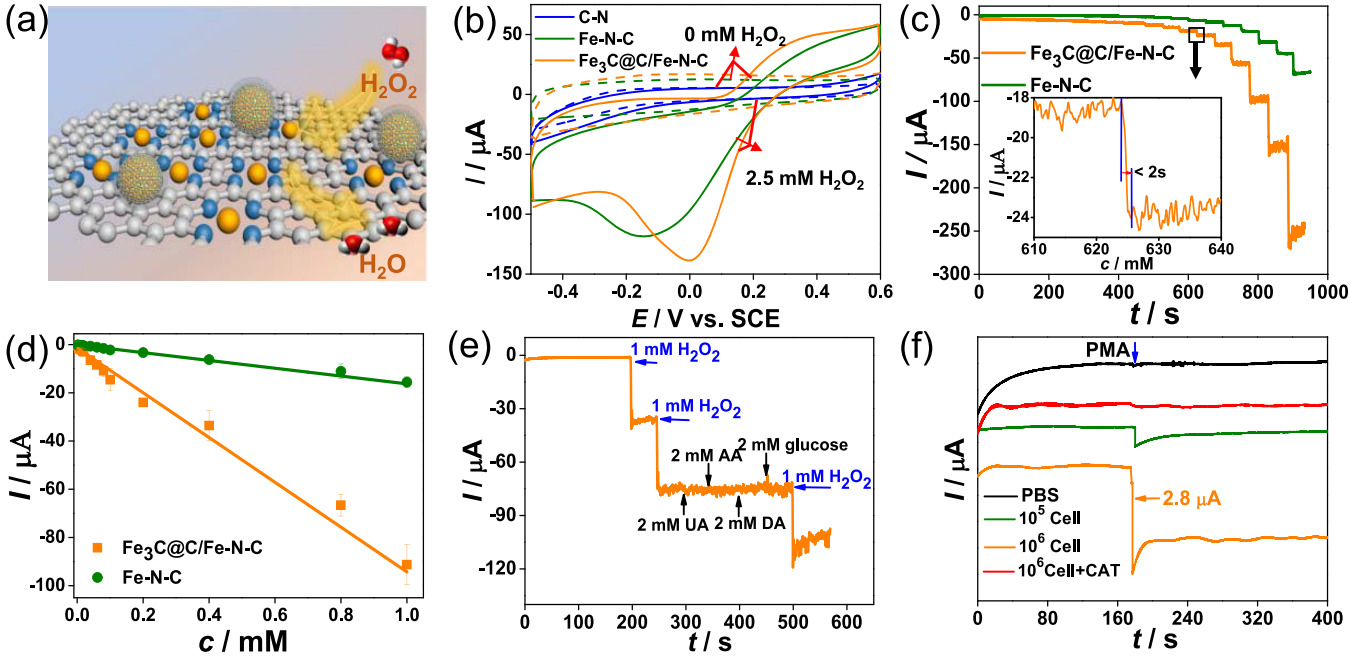


**Figure 5.** (a) Schematic of $Fe_3C$@C/Fe−N−C-based $H_2O_2$ electrochemical sensing. (b) Typical CV curves of C−N, Fe−N−C, and $Fe_3C$@C/Fe−N−C with (full lines) and without (dotted lines) 2.5 mM $H_2O_2$. (c) The amperometric responses of $Fe_3C$@C/Fe−N−C and Fe−N−C to the successive addition of $H_2O_2$ at 0 V. (d) Corresponding calibration curves of current versus $H_2O_2$ concentrations for $Fe_3C$@C/Fe−N−C and Fe−N−C. (e) I−t response current of $Fe_3C$@C/Fe−N−C at 0 V with the successive addition of 1 mM $H_2O_2$, 2 mM UA, 2 mM AA, 2 mM DA, and 2 mM glucose. (f) I−t response of $H_2O_2$ release from Hela cells at 0 V. All tests were carried out in 0.1 M $N_2$-saturated PBS (pH = 7.4).

noteworthy to improve the POD-like activity of $Fe_3C$@C/Fe−N−C. Notably, $Fe_3C$@C/Fe−N−C also maintains excellent stability with the temperature variation, demonstrating that it possesses outstanding robustness in harsh environments, providing potential in practice (Figure S8).

Given the excellent POD-like activity of $Fe_3C$@C/Fe−N−C, it is expected to serve as advanced electrode materials for the sensitive sensing of $H_2O_2$ (Figure 5a). Before the evaluation of the capacity of electrocatalytic $H_2O_2$, the electrochemical properties of Fe−N−C- and $Fe_3C$@C/Fe−N−C-modified GCE were first observed. As depicted in Figure S9, the redox peak of the cyclic voltammetry (CV) curve for $Fe_3C$@C/Fe−N−C is the largest accompanied by a small peak potential separation ($\Delta E_p$). According to the Randles−Sevcik equation, the electrochemical active areas of $Fe_3C$@C/Fe−N−C, Fe−N−C, and GCE are calculated to be 0.0601, 0.0489,


https://doi.org/10.1021/acs.analchem.1c00635
Anal. Chem. 2021, 93, 5334−5342

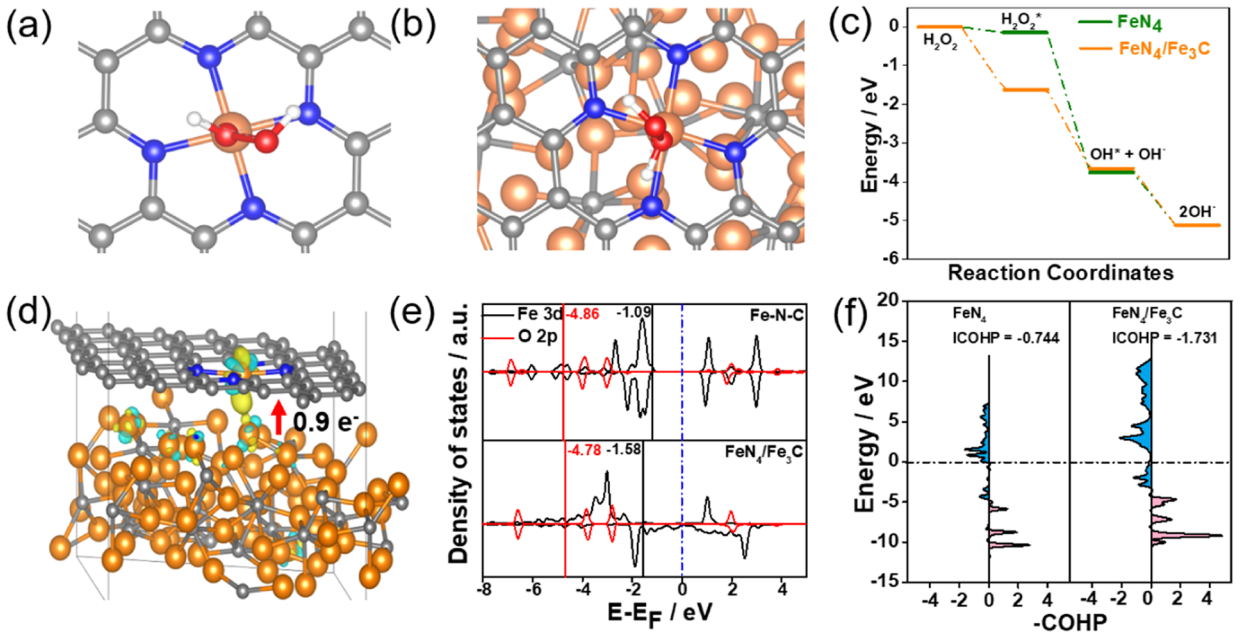


**Figure 6.** Adsorption configuration of $H_2O_2$ on the surfaces of $FeN_4$ (a) and $FeN_4/Fe_3C$ (b) models. (c) Reaction energy diagram of the reduction of $H_2O_2$ in the $FeN_4$ and $FeN_4/Fe_3C$ models. (d) The differential charge density diagram at the interface of $FeN_4$ sites and $Fe_3C$ in $FeN_4/Fe_3C$ models. (e) The PDOS of O and Fe. (f) The pCOHP for the $FeN_4$ and $FeN_4/Fe_3C$ models with $H_2O_2$ adsorbates.

and 0.0416 $cm^2$, respectively, illustrating the largest electrochemical active area of $Fe_3C$@C/Fe−N−C.[37] Electrochemical impedance spectroscopy (EIS) spectra show that $Fe_3C$@C/Fe−N−C also exhibits the most outstanding electron transferability with a small semicircular portion at high frequencies (Figure S10).[38] Besides, the linear sweep voltammetry (LSV) curves shown in Figure S11 illustrate that both $Fe_3C$@C/Fe−N−C and Fe−N−C have wide potential windows (~2.50 V) in comparison to the bare GCE, ensuring that the current signals of $H_2O_2$ detection are not affected.

The catalytic activity of the obtained catalysts toward $H_2O_2$ was assessed in 0.1 M $N_2$-saturated PBS (pH = 7.4) (Figure 5a). As shown in Figure 5b, compared with C−N, Fe−N−C generates a remarkable reduction current, indicating the outstanding $H_2O_2$ reduction activity. Impressively, with the further introduction of $Fe_3C$@C, $Fe_3C$@C/Fe−N−C delivers a much higher reduction current with a reduction peak of 0 V than Fe−N−C. With the increasing concentrations of $H_2O_2$, the peak currents of $Fe_3C$@C/Fe−N−C and Fe−N−C gradually increase, indicating that the changes in current are derived from the reduction of $H_2O_2$ (Figure S12). This result illustrates that $Fe_3C$@C plays an important role in improving the reduction ability of $H_2O_2$ for single atomic Fe sites. To explore the role of $Fe_3C$@C, we also evaluate the performance of $Fe_3C$@C (Figure S13). Accordingly, $Fe_3C$@C is poor in the $H_2O_2$ reduction, with a slight current signal change after the injection of $H_2O_2$. This result illustrates that the synergistic effect between Fe−N−C and $Fe_3C$@C is derived from the modulation of the electronic structures of single atomic Fe sites by $Fe_3C$@C, rather than the superposition of these two sites. Furthermore, the detection sensitivity of $Fe_3C$@C/Fe−N−C and Fe−N−C toward $H_2O_2$ was examined by real-time I−t curves at a constant potential of 0 V upon successive addition of $H_2O_2$. As shown in Figure 5c, $Fe_3C$@C/Fe−N−C delivers a more significant current change for the successive addition of $H_2O_2$ than Fe−N−C and has a current response even with the injection of 1 $\mu$M $H_2O_2$ (Figure S14), confirming the high electrocatalytic ability of $Fe_3C$@C/Fe−N−C. The inset in Figure 5c displays the fast response (less than 2 s) of $Fe_3C$@C/Fe−N−C toward $H_2O_2$. In Figure 5d, the linear current response of the calibration curves of current versus $H_2O_2$ concentrations of $Fe_3C$@C/Fe−N−C ranges from 1 $\mu$M to 6000 $\mu$M with a sensitivity of 1225 $\mu A \cdot mM^{-1} \cdot cm^{-2}$ and an LOD (3 s/k) of 0.26 $\mu$M, which are superior to those of Fe−N−C (210.28 $\mu A \cdot mM^{-1} \cdot cm^{-2}$ and 0.84 $\mu$M). Moreover, compared with the reported catalysts listed in Table S5, $Fe_3C$@C/Fe−N−C also shows outstanding $H_2O_2$ detection performance in terms of LOD, response time, and linear range.[27,39−46]

As for a practical biosensor, much more importance should also be attached to the selectivity.[47,48] Especially, obvious current responses can be observed for $Fe_3C$@C/Fe−N−C whenever 1 mM $H_2O_2$ was injected, while there are almost no changes with the addition of a series of interferents including uric acid (UA), ascorbic acid (AA), dopamine (DA), and glucose despite their concentrations are two-fold that of $H_2O_2$ (Figure 5e). More importantly, the current response of $H_2O_2$ is not disturbed in the presence of all of the above interferents, indicating the good selectivity to $H_2O_2$ as well as the anti-interference ability to some common biologically active substances of $Fe_3C$@C/Fe−N−C. Furthermore, the repeatability of $Fe_3C$@C/Fe−N−C for $H_2O_2$ detection was evaluated through the I−t measurements with five successive injections of $H_2O_2$ at 0 V (Figure S15). The calculated relative standard deviation (RSD) of the current is less than 3.60%. Similarly, the reproducibility was also carried out by the same way in five independent sensors, where the RSD is calculated as 4.8%. These results manifest the satisfactory repeatability and reproducibility of $Fe_3C$@C/Fe−N−C. As shown in Figure S16, there are almost no changes in current during the long-term test for both $Fe_3C$@C/Fe−N−C and Fe−N−C, displaying their excellent stability.

By taking advantage of high sensitivity, selectivity, and stability, $Fe_3C$@C/Fe−N−C was used to detect $H_2O_2$ released


https://doi.org/10.1021/acs.analchem.1c00635
Anal. Chem. 2021, 93, 5334−5342

by Hela cells. PMA is used to stimulate cells to generate $H_2O_2$. As shown in Figure 5f, there is no current change for the PBS solution (black line) when PMA is injected. With $10^5$ Hela cells, the current increases significantly after the addition of PMA (green line). With a further increase in the number of cells to $10^6$, a more obvious response can be found (the orange line). However, when catalase (CAT) was added to PBS in advance (the red line), the current remained nearly constant because of the consumption of $H_2O_2$ by CAT. The current change is about 2.8 $\mu$A for $10^6$ cells upon the injection of PMA, roughly corresponding to a $H_2O_2$ concentration of 0.05 mM according to the standard curve in Figure 5f. The number of $H_2O_2$ molecules released from each Hela cell is calculated to be about $9 \times 10^{10}$, consistent with the reported value earlier.[49,50] These investigations demonstrate that $Fe_3C$@C/Fe−N−C is a sensitive and reliable probe for the detection of intracellular $H_2O_2$.

To understand the role of $Fe_3C$ nanocrystals in the electrochemical detection of $H_2O_2$ for $Fe_3C$@C/Fe−N−C, we further investigated the underlying mechanism by DFT calculations. The computational details are provided in the Experimental Procedure Section. Typically, two models, namely, $FeN_4$ and $FeN_4/Fe_3C$ with the (211) lattice fringes of $Fe_3C$ were constructed (Figure S17). Figure 6a,b display the adsorption configurations of $H_2O_2$ on the surfaces of $FeN_4$ and $FeN_4/Fe_3C$ and Figure S18 shows the reaction path of $H_2O_2$ reduction in $FeN_4/Fe_3C$.[5,51,52] Regarding the free energy profile, the corresponding adsorption energies of $H_2O_2$ on single atomic Fe sites in $FeN_4$ and $FeN_4/Fe_3C$ are calculated as −0.15 and −1.61 eV (Figure 6c). The lengths of a series of bonds shown in Figure S19 before and after the adsorption of $H_2O_2$ on $FeN_4$ and $FeN_4/Fe_3C$ models are listed in Table S6. As we can see, the Fe−O bond length in the $FeN_4/Fe_3C$ model (2.245 Å) is smaller than that in the $FeN_4$ model (2.774 Å), which is consistent with its larger $H_2O_2$ adsorption energy. Notably, in comparison with the isolated $H_2O_2$ molecules, the O−O bonds of the adsorbed ones are elongated from 1.466 to 1.480 Å ($FeN_4/Fe_3C$) and 1.473 Å ($FeN_4$), respectively, indicating that $H_2O_2$ molecules can be readily dissociated on catalysts, and the introduction of $Fe_3C$ can better activate the adsorbed $H_2O_2$ molecules, resulting in a more efficient $H_2O_2$ reduction activity on $FeN_4/Fe_3C$. Then, the charge transfer between $FeN_4$ sites and $Fe_3C$ was examined to further explore the interaction between $FeN_4$ sites and $Fe_3C$. As illustrated in Figure 6d, the electrons can flow into the $FeN_4$ site from the bottom $Fe_3C$ layer with the decrease of the oxidation state of Fe in the $FeN_4$ site from +1.09 ($FeN_4$) to +0.9 ($FeN_4/Fe_3C$) (Table S7).[53] This kind of modulation of the electronic structure toward the $FeN_4$ site has potential to regulate the interaction between the single atomic Fe sites and reactants or intermediates. The project electronic density of states (PDOS) of $H_2O_2$ adsorption on $FeN_4$ and $FeN_4/Fe_3C$ was calculated (Figure 6e). Especially, the large overlap of the Fe 3d and O 2p orbitals in $FeN_4/Fe_3C$ can be illustrated by the small distance between them. Through the projected crystal orbital Hamilton population (pCOHP), the details of the interaction between Fe and $H_2O_2$ adsorbates were explored, where the positive (pink area) and negative (blue area) sections represent the bond contributions and antibond contributions, respectively. As shown in Figure 6f, by calculating the energy of the pCOHP integral up to the Fermi level, the integrated COHP values (ICHOP) were obtained. Especially, the integrated ICHOP values for $FeN_4$ and $FeN_4/Fe_3C$ with $H_2O_2$ are −0.744 and −1.731, indicating that $FeN_4/Fe_3C$ is more preferred to adsorb $H_2O_2$. In general, the calculation results suggest the important role of $Fe_3C$, which endows $Fe_3C$@C/Fe−N−C with superior $H_2O_2$ reduction activity by improving the $H_2O_2$ adsorption energy in the single atomic Fe sites.

## CONCLUSIONS

In summary, we synthesized Fe SASCs using a facile $C_3N_4$ spatial confinement strategy to produce single atomic Fe sites synergistically enhanced by $Fe_3C$@C nanocrystals. Thanks to the assistance of $Fe_3C$@C nanocrystals, $Fe_3C$@C/Fe−N−C shows superior POD-like activity and delivers excellent $H_2O_2$ detection ability than Fe−N−C. DFT calculations indicate that the intrinsic synergistic effect between $Fe_3C$@C nanocrystals and single atomic Fe sites is derived from the electron transfer from $Fe_3C$@C to single atomic Fe sites, which contributes to the strong adsorption of $H_2O_2$ molecules on single atomic Fe sites. Therefore, these typical SASCs open up a new pathway for the enhanced sensitivity of the detection of $H_2O_2$ in living cells, providing great prospects for further development of $H_2O_2$ electrochemical biosensing. Moreover, due to the unique structure of $Fe_3C$@C/Fe−N−C as well as the optimized electronic and geometric structures SASCs, these synergistically enhanced SASCs may even be extended to other research areas.

## ASSOCIATED CONTENT

### Supporting Information

The Supporting Information is available free of charge at https://pubs.acs.org/doi/10.1021/acs.analchem.1c00635.

Detailed experiment procedures; SEM and $Fe_3C$@C size distribution of $Fe_3C$@C/Fe−N−C; TEM, XPS, XANES, and EXAFS of Fe−N−C; time−absorbance curves of $Fe_3C$@C/Fe−N−C and Fe−N−C; influences of temperature toward the POD-like activity of $Fe_3C$@C/Fe−N−C and Fe−N−C; CV curves, EIS spectra and LSV curves of $Fe_3C$@C/Fe−N−C, Fe−N−C, and $Fe_3C$@C; repeatability, reproducibility, and stability of $Fe_3C$@C/Fe−N−C- and Fe−N−C-based sensors; and DFT details (PDF)

## AUTHOR INFORMATION


### Corresponding Author

**Chengzhou Zhu** − *Key Laboratory of Pesticides and Chemical Biology of Ministry of Education, International Joint Research Center for Intelligent Biosensing Technology and Health, College of Chemistry, Central China Normal University, Wuhan 430079, P. R. China;* orcid.org/0000-0003-0679-7965; Email: czzhu@mail.ccnu.edu.cn

### Authors

**Xiaoqian Wei** − *Key Laboratory of Pesticides and Chemical Biology of Ministry of Education, International Joint Research Center for Intelligent Biosensing Technology and Health, College of Chemistry, Central China Normal University, Wuhan 430079, P. R. China*

**Shaojia Song** − *State Key Laboratory of Heavy Oil Processing, China University of Petroleum, Beijing 102249, P. R. China*

**Weiyu Song** − *State Key Laboratory of Heavy Oil Processing, China University of Petroleum, Beijing 102249, P. R. China;* orcid.org/0000-0001-5720-204X




https://doi.org/10.1021/acs.analchem.1c00635
*Anal. Chem.* 2021, 93, 5334−5342

**Weiqing Xu** − *Key Laboratory of Pesticides and Chemical Biology of Ministry of Education, International Joint Research Center for Intelligent Biosensing Technology and Health, College of Chemistry, Central China Normal University, Wuhan 430079, P. R. China*

**Lei Jiao** − *Key Laboratory of Pesticides and Chemical Biology of Ministry of Education, International Joint Research Center for Intelligent Biosensing Technology and Health, College of Chemistry, Central China Normal University, Wuhan 430079, P. R. China*

**Xin Luo** − *Key Laboratory of Pesticides and Chemical Biology of Ministry of Education, International Joint Research Center for Intelligent Biosensing Technology and Health, College of Chemistry, Central China Normal University, Wuhan 430079, P. R. China*

**Nannan Wu** − *Key Laboratory of Pesticides and Chemical Biology of Ministry of Education, International Joint Research Center for Intelligent Biosensing Technology and Health, College of Chemistry, Central China Normal University, Wuhan 430079, P. R. China*

**Hongye Yan** − *Key Laboratory of Pesticides and Chemical Biology of Ministry of Education, International Joint Research Center for Intelligent Biosensing Technology and Health, College of Chemistry, Central China Normal University, Wuhan 430079, P. R. China*

**Xiaosi Wang** − *Key Laboratory of Pesticides and Chemical Biology of Ministry of Education, International Joint Research Center for Intelligent Biosensing Technology and Health, College of Chemistry, Central China Normal University, Wuhan 430079, P. R. China*

**Wenling Gu** − *Key Laboratory of Pesticides and Chemical Biology of Ministry of Education, International Joint Research Center for Intelligent Biosensing Technology and Health, College of Chemistry, Central China Normal University, Wuhan 430079, P. R. China*

**Lirong Zheng** − *Beijing Synchrotron Radiation Facility, Institute of High Energy Physics, Chinese Academy of Sciences, Beijing 100049, P. R. China*

Complete contact information is available at: https://pubs.acs.org/10.1021/acs.analchem.1c00635

### Author Contributions

[‖]X.W. and S.S. contributed equally to this work.

### Notes

The authors declare no competing financial interest.

## ■ ACKNOWLEDGMENTS

The authors gratefully acknowledge the financial support of the National Natural Science Foundation of China (Nos. 22074049, 22004042, and 21503273), the Fundamental Research Funds for the Central Universities (CCNU20QN007 and CCNU20TS013), and the Program of Introducing Talents of Discipline to Universities of China (111 program, B17019). The authors thank the 1W1B station in Beijing Synchrotron Radiation Facility (BSRF) for X-ray absorption spectroscopy measurements.

## ■ REFERENCES

(1) Updike, S.; Hicks, G. *Nature* **1967**, *214*, 986.
(2) Kornienko, N.; Ly, K. H.; Robinson, W. E.; Heidary, N.; Zhang, J. Z.; Reisner, E. *Acc. Chem. Res.* **2019**, *52*, No. 1439.
(3) Sarma, A. K.; Vatsyayan, P.; Goswami, P.; Minteer, S. D. *Biosens. Bioelectron.* **2009**, *24*, 2313.
(4) Jiao, L.; Xu, W.; Wu, Y.; Yan, H.; Gu, W.; Du, D.; Lin, Y.; Zhu, C. *Chem. Soc. Rev.* **2021**, *50*, 750−765.
(5) Wu, P.; Cai, Z.; Chen, J.; Zhang, H.; Cai, C. *Biosens. Bioelectron.* **2011**, *26*, 4012.
(6) Sun, X.; Guo, S.; Liu, Y.; Sun, S. *Nano Lett.* **2012**, *12*, 4859.
(7) Zhang, W.; Fan, G.; Yi, H.; Jia, G.; Li, Z.; Yuan, C.; Bai, Y.; Fu, D. *Small* **2018**, *14*, No. 1703713.
(8) Tan, H.; Tang, J.; Henzie, J.; Li, Y.; Xu, X.; Chen, T.; Wang, Z.; Wang, J.; Ide, Y.; Bando, Y.; Yamauchi, Y. *ACS Nano* **2018**, *12*, 5674−5683.
(9) Yin, P.; Yao, T.; Wu, Y.; Zheng, L.; Lin, Y.; Liu, W.; Ju, H.; Zhu, J.; Hong, X.; Deng, Z.; Zhou, G.; Wei, S.; Li, Y. *Angew. Chem., Int. Ed.* **2016**, *55*, 10800.
(10) Yang, X.; Chen, C.; Zhou, Z.; Sun, S. *Acta Phys. Chim. Sin.* **2019**, *35*, 472−485.
(11) Cao, L.; Luo, Q.; Liu, W.; Lin, Y.; Liu, X.; Cao, Y.; Zhang, W.; Wu, Y.; Yang, J.; Yao, T.; Wei, S. *Nat. Catal.* **2019**, *2*, 134.
(12) Zheng, T.; Jiang, K.; Ta, N.; Hu, Y.; Zeng, J.; Liu, J.; Wang, H. *Joule* **2019**, *3*, 265.
(13) Gong, Y.-N.; Jiao, L.; Qian, Y.; Pan, C. Y.; Zheng, L.; Cai, X. B.; Liu, S.; Yu, H.; Jiang, H. L. *Angew. Chem.* **2020**, *132*, 2727.
(14) Hülsey, M. J.; Zhang, B.; Ma, Z.; Asakura, H.; Do, D. A.; Chen, W.; Tanaka, T.; Zhang, P.; Wu, Z.; Yan, N. *Nat. Commun.* **2019**, *10*, No. 1330.
(15) Gu, W.; Wang, H.; Jiao, L.; Wu, Y.; Chen, Y.; Hu, L.; Gong, J.; Du, D.; Zhu, C. *Angew. Chem., Int. Ed.* **2020**, *59*, 3534.
(16) Hou, H.; Mao, J.; Han, Y.; Wu, F.; Zhang, M.; Wang, D.; Mao, L.; Li, Y. *Sci. China Chem.* **2019**, *62*, 1720.
(17) Li, Z.; Chen, Y.; Ji, S.; Tang, Y.; Chen, W.; Li, A.; Zhao, J.; Xiong, Y.; Wu, Y.; Gong, Y.; Yao, T.; Liu, W.; Zheng, L.; Dong, J.; Wang, Y.; Zhuang, Z.; Xing, W.; He, C. T.; Peng, C.; Cheong, W. C.; Li, Q.; Zhang, M.; Chen, Z.; Fu, N.; Gao, X.; Zhu, W.; Wan, J.; Zhang, J.; Gu, L.; Wei, S.; Hu, P.; Luo, J.; Li, J.; Chen, C.; Peng, Q.; Duan, X.; Huang, Y.; Chen, X. M.; Wang, D.; Li, Y. *Nat. Chem.* **2020**, *12*, 764.
(18) Guo, X.; Fang, G.; Li, G.; Ma, H.; Fan, H.; Yu, L.; Ma, C.; Wu, X.; Deng, D.; Wei, M.; Tan, D.; Si, R.; Zhang, S.; Li, J.; Sun, L.; Tang, Z.; Pan, X.; Bao, X. *Science* **2014**, *344*, 616.
(19) Yuan, K.; Lutzenkirchen-Hecht, D.; Li, L.; Shuai, L.; Li, Y.; Cao, R.; Qiu, M.; Zhuang, X.; Leung, M. K. H.; Chen, Y.; Scherf, U. *J. Am. Chem. Soc.* **2020**, *142*, 2404.
(20) Zhang, H.; Chung, H. T.; Cullen, D. A.; Wagner, S.; Kramm, U. I.; More, K. L.; Zelenay, P.; Wu, G. *Energy Environ. Sci.* **2019**, *12*, 2548.
(21) Gong, L.; Zhang, H.; Wang, Y.; Luo, E.; Li, K.; Gao, L.; Wang, Y.; Wu, Z.; Jin, Z.; Ge, J.; Jiang, Z.; Liu, C.; Xing, W. *Angew. Chem., Int. Ed.* **2020**, *59*, 13923.
(22) Jiang, W. J.; Gu, L.; Li, L.; Zhang, Y.; Zhang, X.; Zhang, L. J.; Wang, J. Q.; Hu, J. S.; Wei, Z.; Wan, L. J. *J. Am. Chem. Soc.* **2016**, *138*, 3570.
(23) Sun, X.; Wei, P.; Gu, S.; Zhang, J.; Jiang, Z.; Wan, J.; Chen, Z.; Huang, L.; Xu, Y.; Fang, C.; Li, Q.; Han, J.; Huang, Y. *Small* **2019**, *16*, No. 1906057.
(24) Wei, X.; Song, S.; Wu, N.; Luo, X.; Zheng, L.; Jiao, L.; Wang, H.; Fang, Q.; Hu, L.; Gu, W.; Song, W.; Zhu, C. *Nano Energy* **2021**, No. 105840.
(25) Wei, X.; Luo, X.; Wu, N.; Gu, W.; Lin, Y.; Zhu, C. *Nano Energy* **2021**, No. 105817.
(26) Liu, D.; Wu, C.; Chen, S.; Ding, S.; Xie, Y.; Wang, C.; Wang, T.; Haleem, Y. A.; Rehman, Z.; Sang, Y.; Liu, Q.; Zheng, X.; Wang, Y.; Ge, B.; Xu, H.; Song, L. *Nano Res.* **2018**, *11*, 2217.
(27) Li, Z.; Wei, L.; Jiang, W. J.; Hu, Z.; Luo, H.; Zhao, W.; Xu, T.; Wu, W.; Wu, M.; Hu, J. S. *Appl. Catal., B* **2019**, *251*, 240−246.
(28) Xia, W.; Tang, J.; Li, J.; Zhang, S.; Wu, K. C. W.; He, J.; Yamauchi, Y. *Angew. Chem., Int. Ed.* **2019**, *58*, 13354−13359.
(29) Guo, Y.; Tang, J.; Henzie, J.; Jiang, B.; Qian, H.; Wang, Z.; Tan, H.; Bando, Y.; Yamauchi, Y. *Mater. Horiz.* **2017**, *4*, 1171−1177.

(30) Luo, X.; Wei, X.; Wang, H.; Gu, W.; Kaneko, T.; Yoshida, Y.; Zhao, X.; Zhu, C. *Nano-Micro Lett.* **2020**, *12*, No. 163.
(31) Cao, L.; Lin, Z.; Huang, J.; Yu, X.; Wu, X.; Zhang, B.; Zhan, Y.; Xie, F.; Zhang, W.; Chen, J.; Xie, W.; Mai, W.; Meng, H. *Int. J. Hydrogen Energy* **2017**, *42*, 876.
(32) Zhu, C.; Shi, Q.; Xu, B. Z.; Fu, S.; Wan, G.; Yang, C.; Yao, S.; Song, J.; Zhou, H.; Du, D.; Beckman, S. P.; Su, D.; Lin, Y. *Adv. Energy Mater.* **2018**, *8*, No. 1801956.
(33) Wang, H.; Yin, F. X.; Liu, N.; Kou, R. H.; He, X. B.; Sun, C. J.; Chen, B. H.; Liu, D. J.; Yin, H. Q. *Adv. Funct. Mater.* **2019**, *29*, No. 1901531.
(34) Gan, G.; Li, X.; Wang, L.; Fan, S.; Mu, J.; Wang, P.; Chen, G. *ACS Nano* **2020**, *14*, 9929.
(35) Jiang, R.; Li, L.; Sheng, T.; Hu, G.; Chen, Y.; Wang, L. *J. Am. Chem. Soc.* **2018**, *140*, 11594.
(36) Jiang, B.; Duan, D. M.; Gao, L. Z.; Zhou, M. J.; Fan, K. L.; Tang, Y.; Xi, J. Q.; Bi, Y. H.; Tong, Z.; Gao, G. G. F.; Xie, N.; Tang, A. F.; Nie, G. H.; Liang, M. M.; Yan, X. Y. *Nat. Protoc.* **2018**, *13*, 1506.
(37) Xue, W.; Bo, X.; Zhou, M.; Guo, L. *J. Electroanal. Chem.* **2016**, *781*, 204.
(38) Ke, X.; Zhu, G.; Dai, Y.; Shen, Y.; Yang, J.; Liu, J. *J. Electroanal. Chem.* **2018**, *817*, 176.
(39) Song, M.; Wang, J.; Chen, B.; Wang, L. *Anal. Chem.* **2017**, *89*, 11537.
(40) Balamurugan, J.; Thanh, T. D.; Karthikeyan, G.; Kim, N. H.; Lee, J. H. *Biosens. Bioelectron.,* **2017**, *89*, 970.
(41) Qin, Z.; Zhao, Y.; Lin, L.; Zou, P.; Zhang, L.; Chen, H.; Wang, Y.; Wang, G.; Zhang, Y. *Microchim. Acta* **2017**, *184*, 4513.
(42) Du, S.; Ren, Z.; Wu, J.; Xi, W.; Fu, H. *Nano Res.* **2016**, *9*, 2260.
(43) Zhao, Y.; Huo, D.; Bao, J.; Yang, M.; Chen, M.; Hou, J.; Fa, H.; Hou, C. *Sens. Actuators, B* **2017**, *244*, 1037.
(44) Saravana achari, D.; Santhosh, C.; Deivasegamani, R.; Nivetha, R.; Bhatnagar, A.; Jeong, S. K.; Grace, A. N. *Microchim. Acta* **2017**, *184*, 3223.
(45) Hassan, M.; Jiang, Y.; Bo, X.; Zhou, M. *Talanta* **2018**, *188*, 339.
(46) Zhang, Y.; Bai, X.; Wang, X.; Shiu, K.-K.; Zhu, Y.; Jiang, H. *Anal. Chem.* **2014**, *86*, 9459.
(47) Zhu, C.; Yang, G.; Li, H.; Du, D.; Lin, Y. *Anal. Chem.* **2015**, *87*, 230.
(48) Li, Y.; Huan, K.; Deng, D.; Tang, L.; Wang, J.; Luo, L. *ACS Appl. Mater. Interfaces* **2020**, *12*, 3430.
(49) Zhang, Y.; Wu, C.; Zhou, X.; Wu, X.; Yang, Y.; Wu, H.; Guo, S.; Zhang, J. *Nanoscale* **2013**, *5*, No. 1816.
(50) Chang, H.; Wang, X.; Shiu, K.-K.; Zhu, Y.; Wang, J.; Li, Q.; Chen, B.; Jiang, H. *Biosens. Bioelectron.* **2013**, *41*, 789.
(51) Wu, P.; Qian, Y.; Du, P.; Zhang, H.; Cai, C. *J. Mater. Chem.* **2012**, *22*, No. 6402.
(52) Wu, P.; Cai, Z.; Gao, Y.; Zhang, H.; Cai, C. *Chem. Commun.* **2011**, *47*, No. 11327.
(53) Wang, Y.; Tang, Y.-J.; Zhou, K. *J. Am. Chem. Soc.* **2019**, *141*, 14115.


https://doi.org/10.1021/acs.analchem.1c00635
*Anal. Chem.* 2021, 93, 5334−5342